nature nanotechnology

Supplementary information

https://doi.org/10.1038/s41565-026-02335-6

Depth-robust super-resolution nanofabrication for 3D mesoscopic photonic structures

In the format provided by the authors and unedited

Supplementary Information

Table of Contents

Supplementary Figures **2**

Supplementary Fig. 1. Schematic diagram of the Debye vector diffraction integral theory 2
Supplementary Fig. 2. Optical field distributions of the Gaussian beam at different depths 3
Supplementary Fig. 3. Optical field distributions of the LG beam at different depths 4
Supplementary Fig. 4. Simulated intensity distributions of the axicon-based Bessel beam 5
Supplementary Fig. 5. Simulated intensity distributions of the annular-lens-based Bessel beam 6
Supplementary Fig. 6. Effective excitation efficiency from superimposed optical fields 7
Supplementary Fig. 7. Effective excitation efficiency of STED and AB-STED 8
Supplementary Fig. 8. Sensorless AO optimization and defocus responses 9
Supplementary Fig. 9. Linewidth responses to defocus and spherical aberration 10
Supplementary Fig. 10. Assessment of photoresist stability under 532 nm irradiation 11
Supplementary Fig. 11. Relationship between scanning speed and fabricated linewidth 12
Supplementary Fig. 12. Gratings fabricated at various scanning speeds 13
Supplementary Fig. 13. Linewidth as a function of depletion power at different depths 14
Supplementary Fig. 14. AFM comparison of the axial feature dimensions 15
Supplementary Fig. 15. Gratings fabricated by AB-STED and STED DLW 16
Supplementary Fig. 16. Two-dimensional patterns fabricated at a depth of 160 μm 17
Supplementary Fig. 17. Surface-height maps of curved microstructures 18
Supplementary Fig. 18. Triangular structures fabricated by two writing methods 19
Supplementary Fig. 19. Model of the helix corresponding to Extended Data Fig. 1c,d 20
Supplementary Fig. 20. Top view of the helix structure 21
Supplementary Fig. 21. Nanorod arrays fabricated at different depths 22
Supplementary Fig. 22. Depth-dependent aspect ratio of nanorods 23
Supplementary Fig. 23. Structural views of the 4F system 24
Supplementary Fig. 24. Magnified views of the STED-fabricated 4F system 25
Supplementary Fig. 25. Intensity profiles of the output foci of the 4F systems 26
Supplementary Fig. 26. Structural views of the vortex phase plate 27
Supplementary Fig. 27. Meridional and sagittal modulation transfer functions 28
Supplementary Fig. 28. Through-focus modulation transfer functions of the objective lens 29
Supplementary Fig. 29. Magnified views of the STED-fabricated objective lens 30
Supplementary Fig. 30. Linewidths at a depth of 1400 μm 31
Supplementary Fig. 31. Magnified views of the structures shown in Fig. 5a 32
Supplementary Fig. 32. Molecular structures of photoinitiator DETC and monomer PETTA 33
Supplementary Fig. 33. Absorption spectrum of photoresist 34
Supplementary Fig. 34. Emission spectrum of photoresist 35
Supplementary Fig. 35. Energy levels and optical transitions of the photoinitiator 36

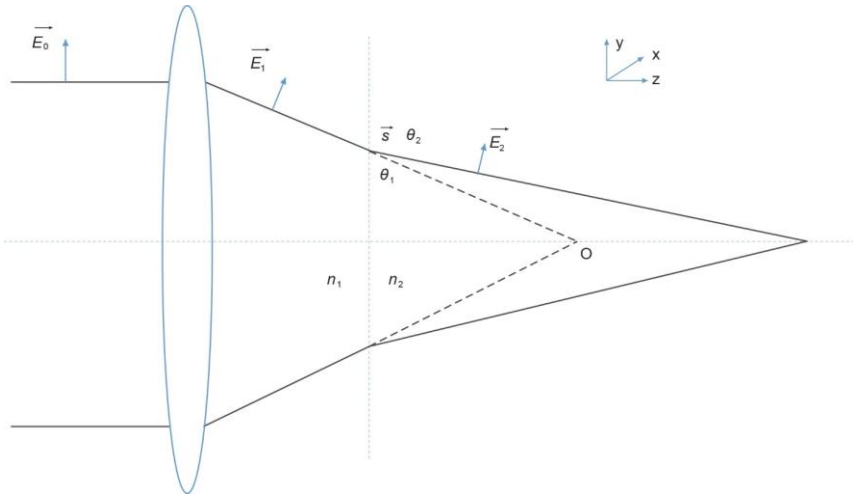
Supplementary Tables **37**

Supplementary Table 1. Simulated axial overlap of Bessel and Gaussian beams 37
Supplementary Table 2. Linewidth comparison at a writing depth of 160 μm 37

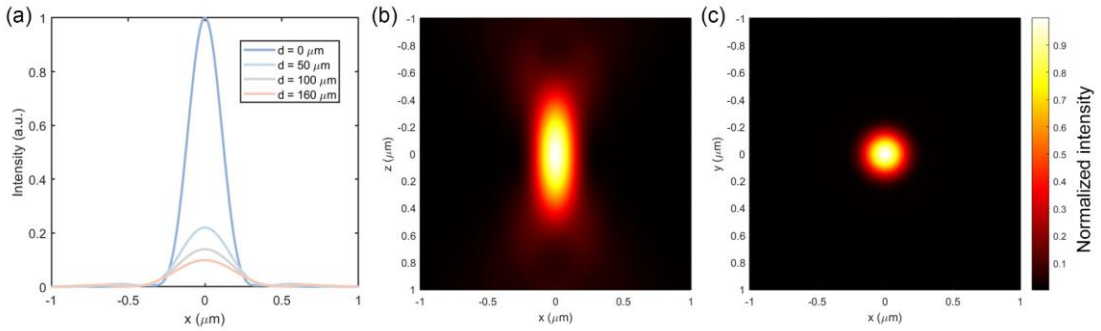
Supplementary Notes **38**

Supplementary Note 1. Debye vector diffraction integral model 38
Supplementary Note 2. Impact of spherical aberration on Gaussian beams 40
Supplementary Note 3. Impact of spherical aberration on the LG beam 40
Supplementary Note 4. First-order Bessel beam generated by an axicon 41
Supplementary Note 5. First-order Bessel beam generated by an annular lens 42
Supplementary Note 6. Adaptive-optics validation of axial matching 43
6.1 Sensorless AO procedure 43
6.2 Linewidth comparison at 160 μm 45
6.3 Tolerance to axial misalignment and spherical aberration 46

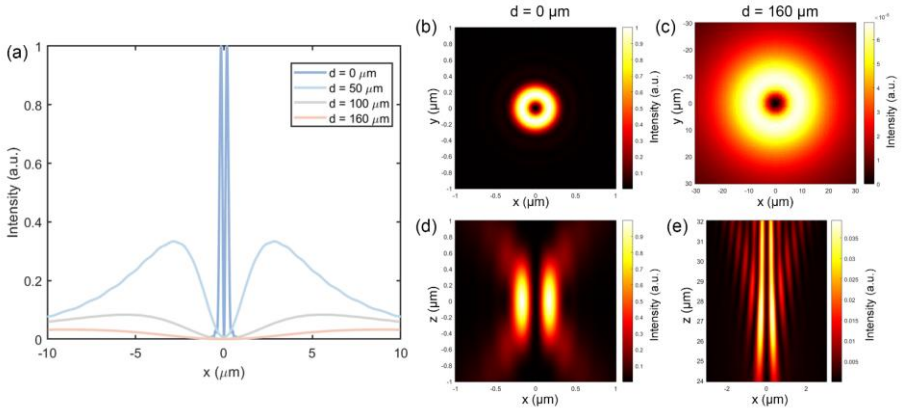
Supplementary References **49**



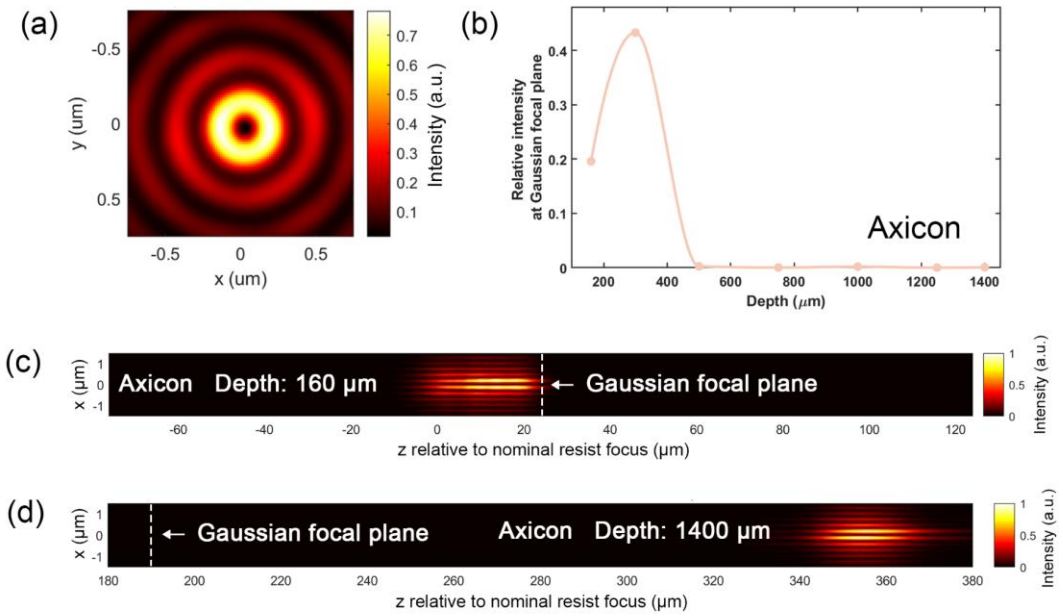
Supplementary Fig. 1. Schematic diagram of the Debye vector diffraction integral theory.



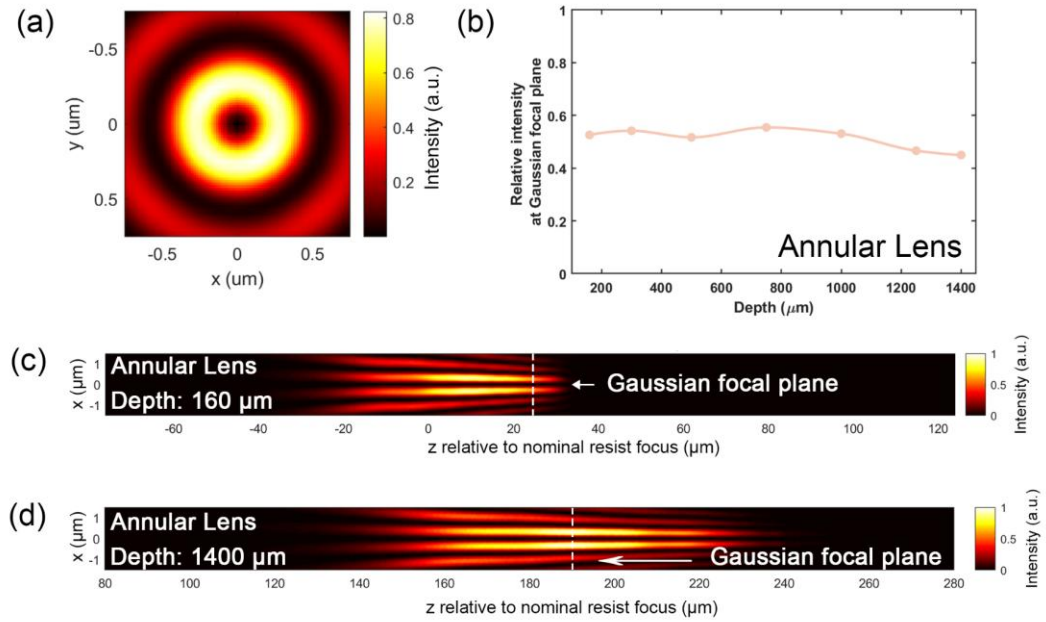
Supplementary Fig. 2. (a) Optical field distributions of the Gaussian beam at different depths. (b) The XZ intensity distribution of Gaussian light at $d = 0\ \mu m$. (c) The XY intensity distribution of Gaussian light at $d = 0\mu m$.



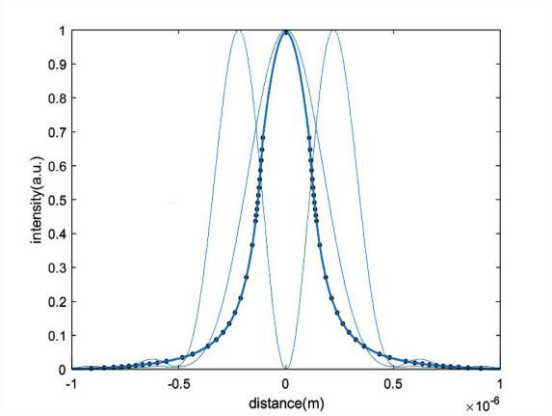
Supplementary Fig. 3. (a) Optical field distributions of Laguerre–Gaussian beam at different depths. To make the intensity peaks more apparent in the plots, all intensities except those at $d = 0\ \mu m$ were multiplied by 500. (b, c) Intensity distribution in the XY plane at $d = 0\ \mu m$ and $d = 160\ \mu m$, respectively. (d, e) Intensity distribution in the XZ plane at $d = 0\ \mu m$ and $d = 160\ \mu m$, respectively.



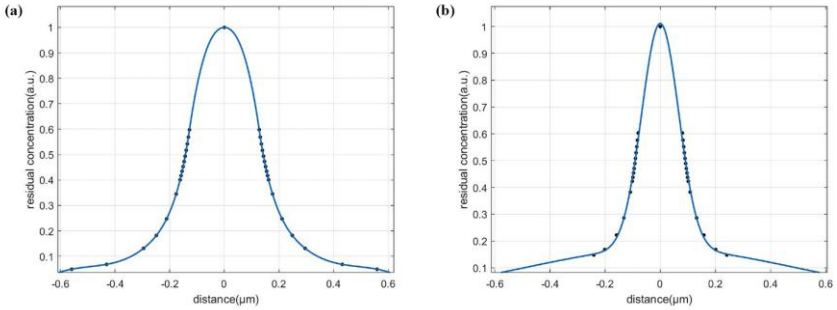
Supplementary Fig. 4. Simulated intensity distributions of the axicon-based Bessel beam. (a) Transverse XY intensity distribution of the axicon-based Bessel beam at $z = 20\ \mu m$ and depth of 160 μm. (b) Relative intensity of the axicon-based Bessel beam at the Gaussian focal plane as a function of fabrication depth. The relative intensity is defined as the first-ring mean intensity, $(\langle |Ex|^2 + |Ey|^2 + |Ez|^2 \rangle_{ring})$, and normalized to the surface reference intensity. (c) Longitudinal XZ intensity distribution of the axicon-based Bessel beam at a depth of 160 μm. (d) Longitudinal XZ intensity distribution of the axicon-based Bessel beam at a depth of 1400 μm.



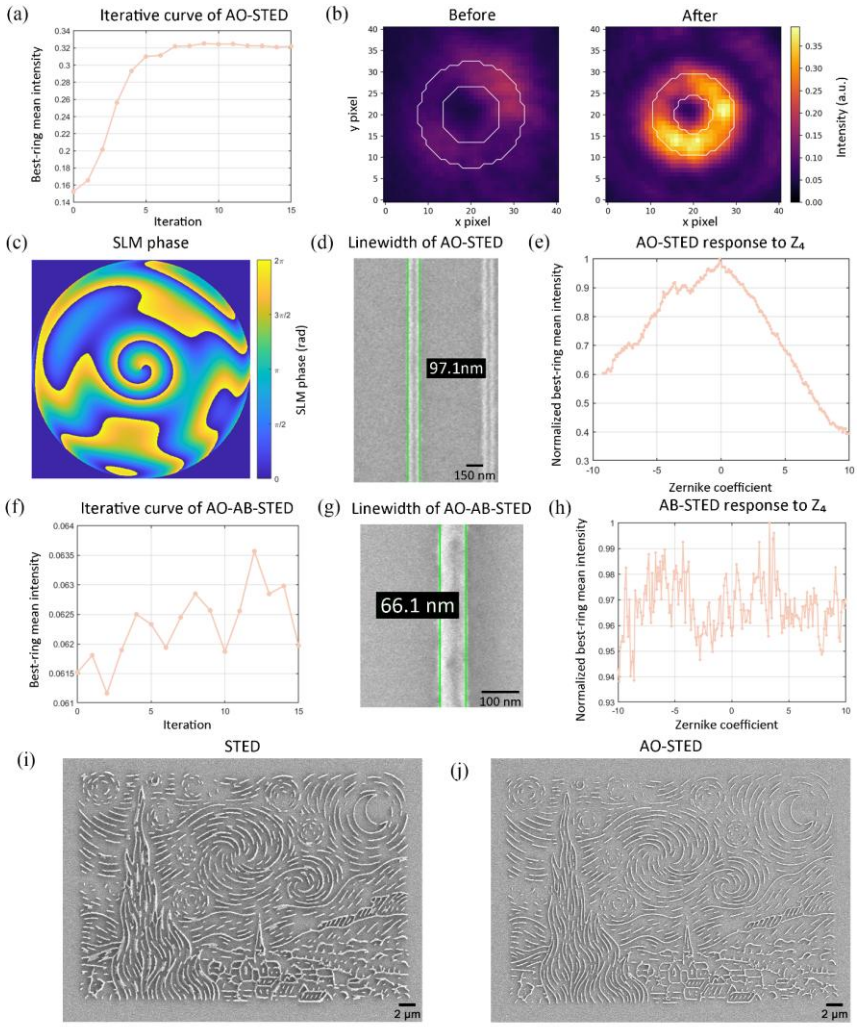
Supplementary Fig. 5. Simulated intensity distributions of the annular-lens-based Bessel beam. (a) Transverse XY intensity distribution of the annular-lens-based Bessel beam at $z = 20\ \mu m$ and depth of 160 μm. (b) Relative intensity of the annular-lens-based Bessel beam at the Gaussian focal plane as a function of fabrication depth. (c) Longitudinal XZ intensity distribution of the annular-lens-based Bessel beam at a depth of 160 μm. (d) Longitudinal XZ intensity distribution of the annular-lens-based Bessel beam at a depth of 1400 μm.



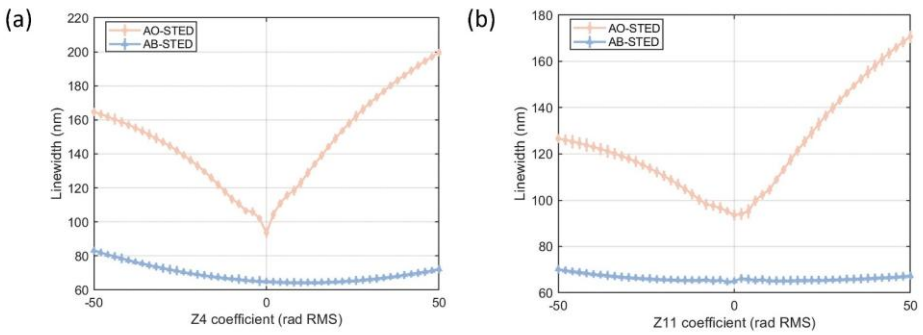
Supplementary Fig. 6. The physical idea of obtaining effective excitation efficiency by superimposing the light field distribution and the depletion efficiency distribution. The light-colored double-peaked curve represents the depletion-beam profile, the light-colored single-peaked curve represents the excitation-beam profile, and the dark-colored curve represents the resulting effective excitation profile under dual-beam superposition.



Supplementary Fig. 7. (a) Effective excitation efficiency employing a Laguerre–Gaussian beam at 100 μm depth. (b) Effective excitation efficiency utilizing a first-order Bessel beam under the same conditions (100 μm depth).



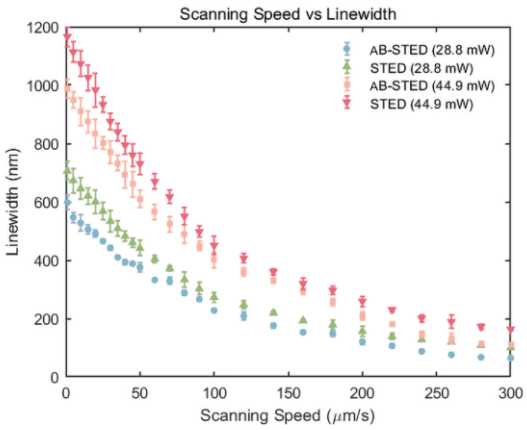
Supplementary Fig. 8. Sensorless adaptive optics optimization and defocus responses at a writing depth of 160 μm (numerical aperture=1.1, working distance=1.5 mm). (a) Best-ring mean intensity during AO-STED optimization, measured from baseline-subtracted camera images and normalization to the 16-bit camera range. (b) Back-reflected depletion doughnut before and after correction. The white contours delineate the annular feedback region. (c) Optimized spatial light modulator phase pattern combining vortex with Zernike corrections. (d) Representative SEM image of a line fabricated by AO-STED. (e) Normalized best-ring mean intensity of AO-STED versus added Z_4 defocus coefficient. (f) Best-ring mean intensity during AB-STED optimization, fluctuating slightly without systematic increase. (g) Representative SEM image of a line fabricated by AO-AB-STED. (h) Normalized best-ring mean intensity of AB-STED versus Z_4 perturbation, showing a nearly constant response. (i, j) SEM images of line-art reproductions of Vincent van Gogh's The Starry Night fabricated by STED (i) and AO-STED (j) DLW.



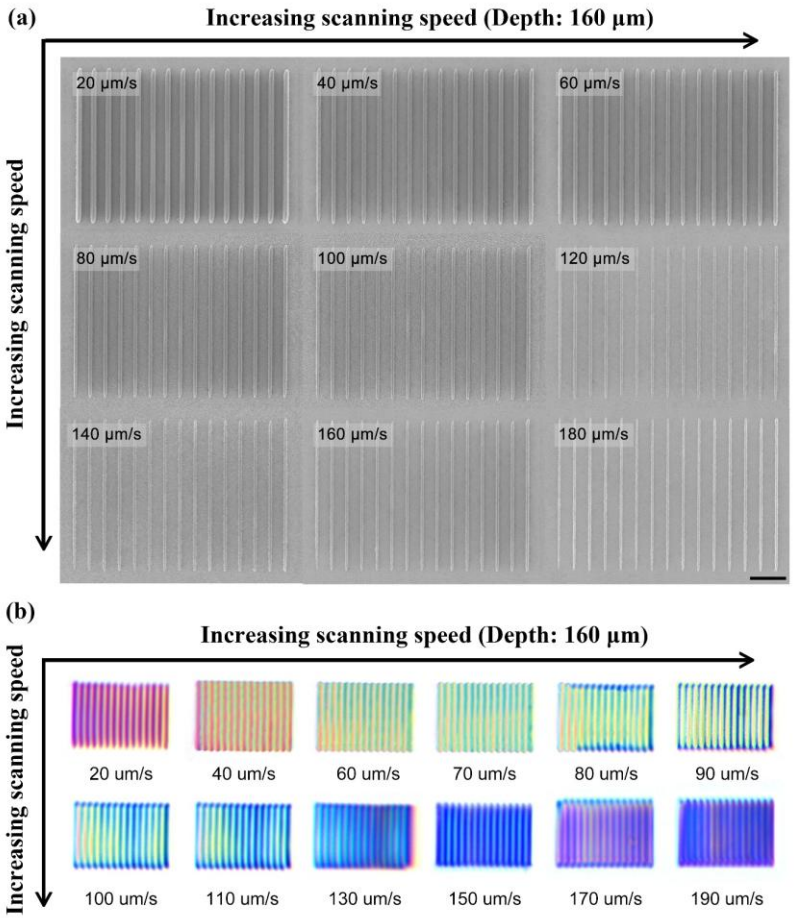
Supplementary Fig. 9. Linewidth responses to controlled (a) Z_4 defocus and (b) Z_{11} primary spherical-aberration perturbations at a writing depth of 160 μm (NA=1.1, WD=1.5 mm). Each additional coefficient was varied from −50 to +50 rad RMS, with the other Zernike coefficients held fixed. Points show mean±s.d. (n=10 independently fabricated lines per coefficient and fabrication method).



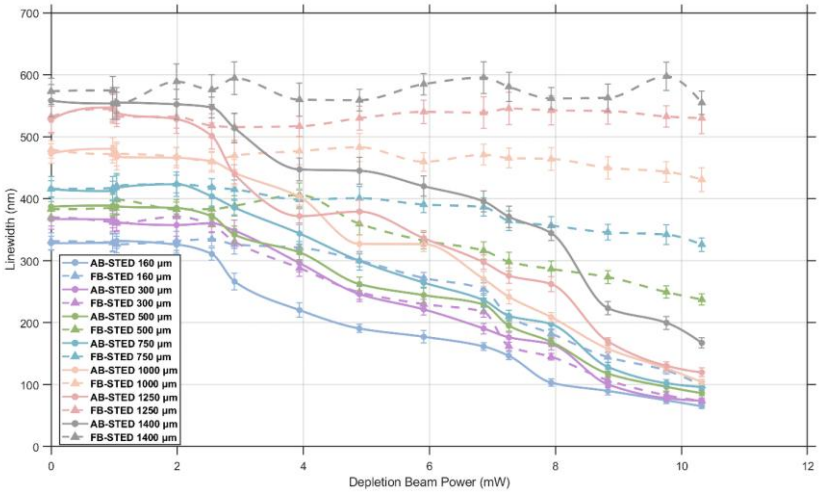
Supplementary Fig. 10. Assessment of photoresist stability under 532 nm irradiation. The black dashed boxes mark the regions exposed to the respective laser beams.



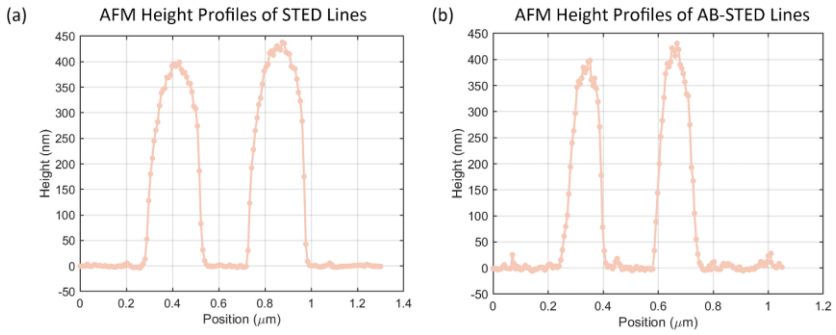
Supplementary Fig. 11. Relationship between scanning speed and fabricated linewidth (numerical aperture=1.27, working distance=0.17 mm). Points show mean±s.d. (n=10 independently fabricated lines per scanning speed, power and fabrication method).



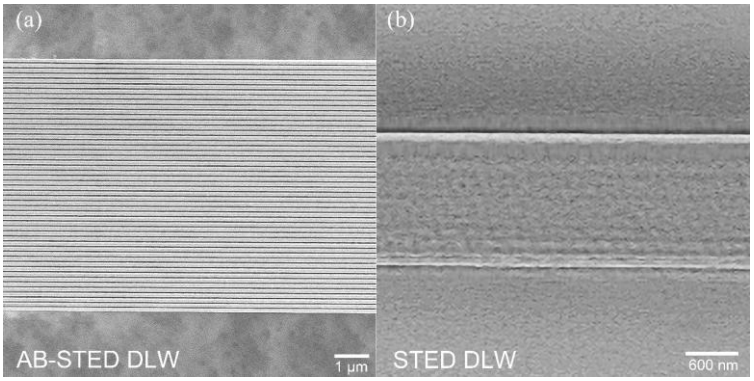
Supplementary Fig. 12. (a) SEM images of gratings fabricated at various scanning speeds (numerical aperture=1.27, working distance=0.17 mm). (b) Structural colors displayed by gratings fabricated at varying scanning speeds (numerical aperture = 1.27, working distance = 0.17 mm).



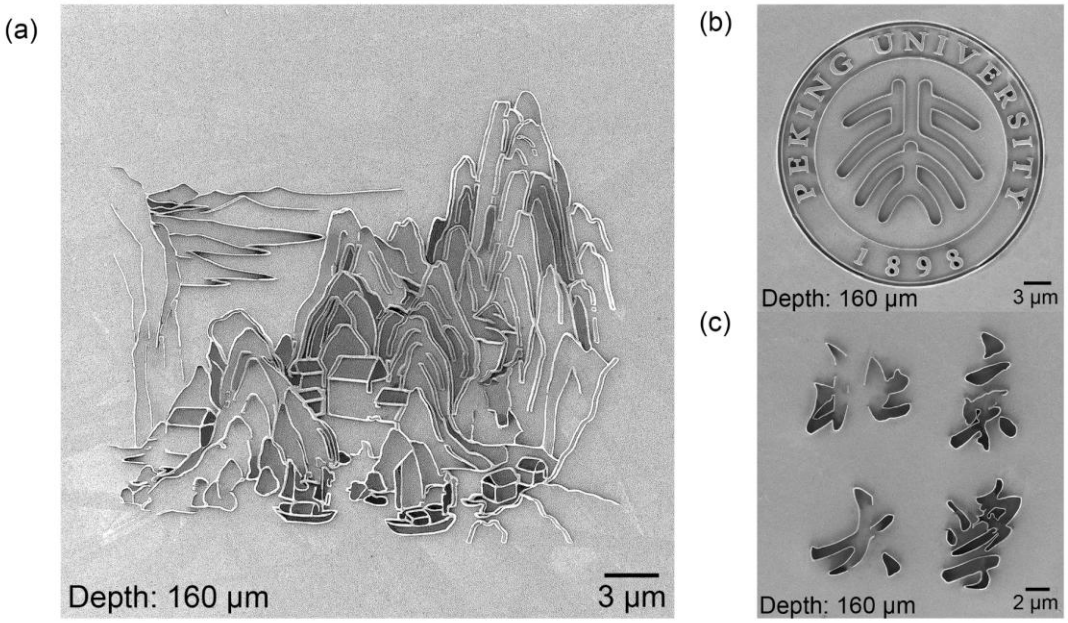
Supplementary Fig. 13. Linewidth as a function of depletion power over depths from 0 to 1400 µm (numerical aperture=1.1, working distance=1.5 mm). Points show mean±s.d. (n=10 independently fabricated lines per condition).



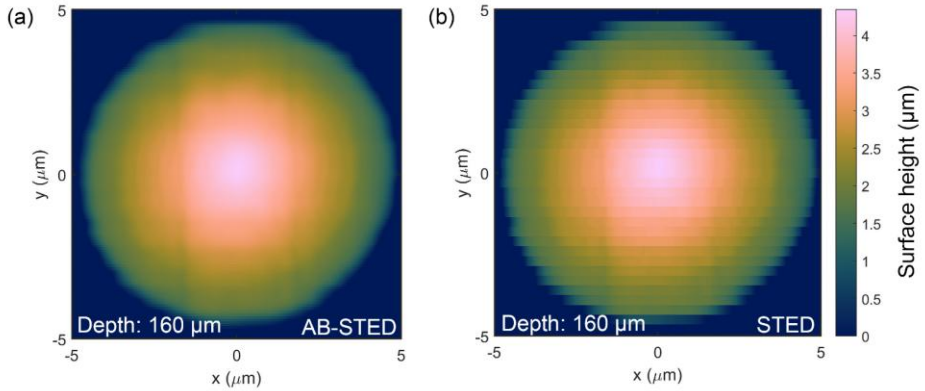
Supplementary Fig. 14. AFM comparison of the axial feature dimensions. AFM height profiles across two representative horizontal lines fabricated at a writing depth of 160 μm using a numerical aperture=1.1, working distance=1.5 mm objective under matched optical powers and writing conditions: (a) STED and (b) AB-STED.



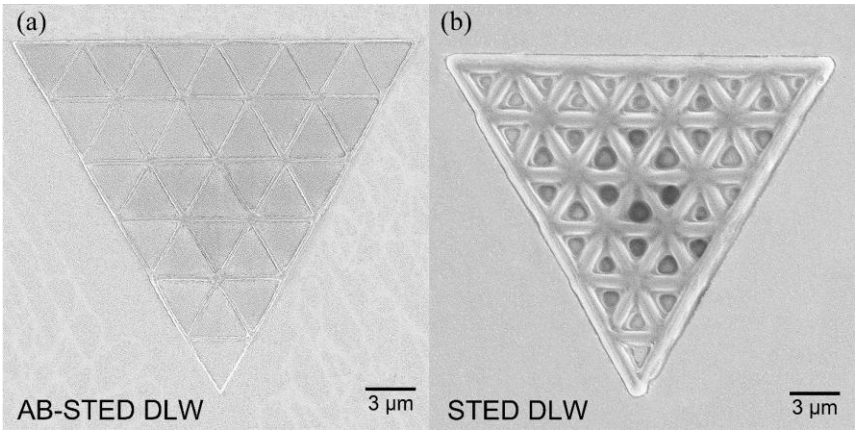
Supplementary Fig. 15. Fabrication results obtained by (a) axially tuneable Bessel beam based stimulated-emission-depletion (AB-STED) direct laser writing (DLW) and (b) STED DLW at a grating period of 150 nm (numerical aperture=1.27, working distance=0.17 mm).



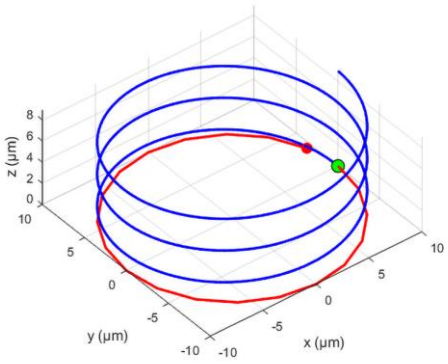
Supplementary Fig. 16. Two-dimensional patterns fabricated at a depth of 160 μm. SEM images of (a) a Chinese landscape painting, (b) the Peking University emblem and (c) the Chinese characters of Peking University, all fabricated by AB-STED direct laser writing (numerical aperture=1.27, working distance=0.17 mm).



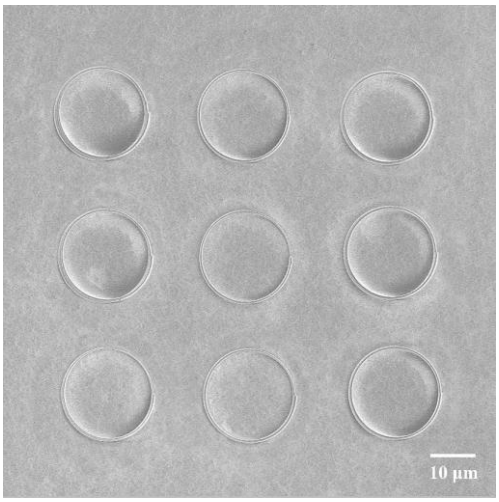
Supplementary Fig. 17. Surface-height maps of curved microstructures fabricated at a depth of 160 µm. Profilometer measurements of identical structures fabricated by (a) AB-STED and (b) STED direct laser writing. The AB-STED-fabricated surface has a smoother, more continuous profile, whereas the STED-fabricated surface shows discrete height bands. The X and Y axes indicate lateral position, and the shared color bar indicates surface height, all in µm.



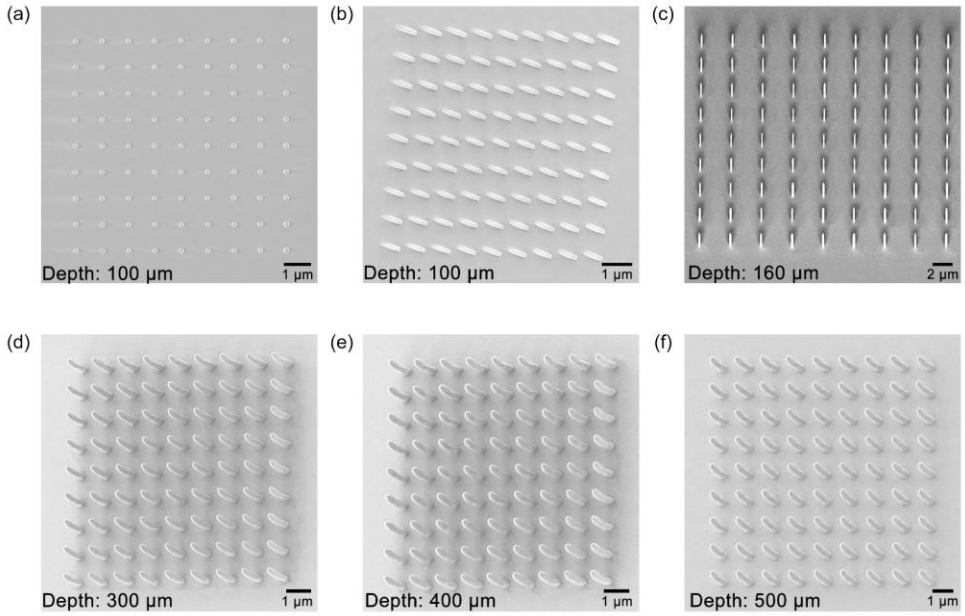
Supplementary Fig. 18. SEM images of triangular structures with a 3 μm thickness fabricated by (a) axially tuneable Bessel beam based stimulated-emission-depletion (AB-STED) and (b) STED direct laser writing (numerical aperture=1.27, working distance=0.17 mm).



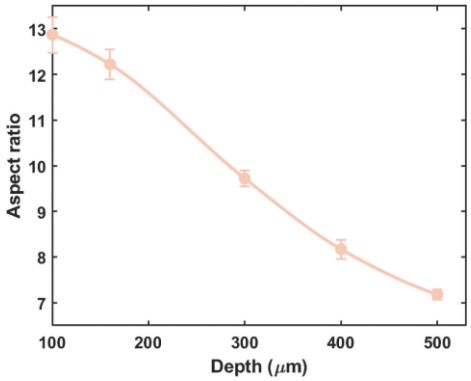
Supplementary Fig. 19. Model of helix of Extended Data Fig. 1c– 1d.



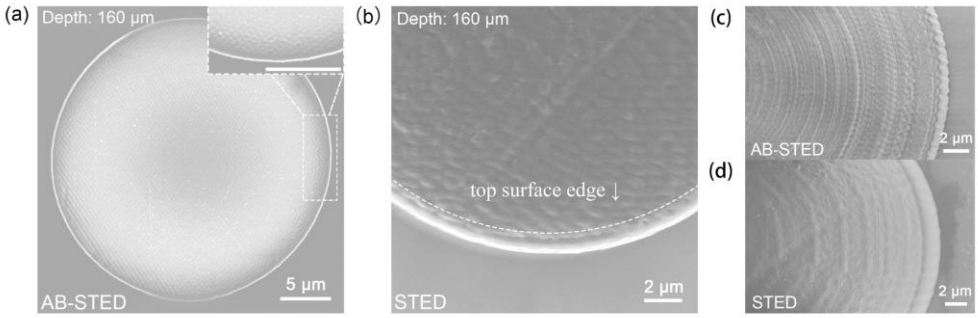
Supplementary Fig. 20. Top view of helix structure (numerical aperture=1.27, working distance=0.17 mm).



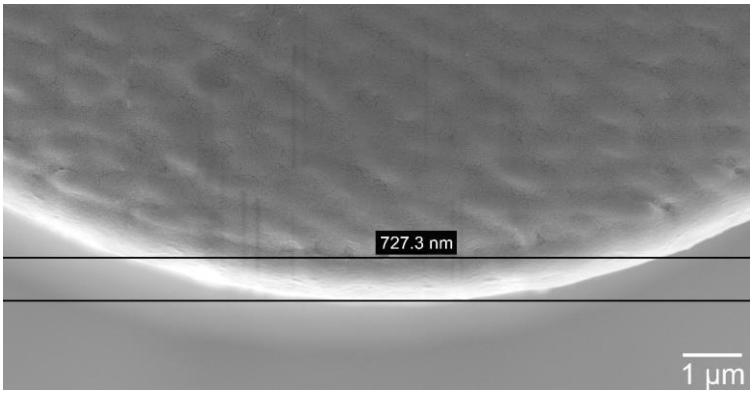
Supplementary Fig. 21. SEM images of nanorod arrays fabricated by axially tuneable Bessel beam based stimulated-emission-depletion (AB-STED) direct laser writing at depths of (a, b) 100 μm, (c) 160 μm, (d) 300 μm, (e) 400 μm, and (f) 500 μm. The results demonstrate the capability of AB-STED direct laser writing to fabricate high-aspect-ratio nanostructures over a large axial depth range (numerical aperture=1.1, working distance=1.5 mm).



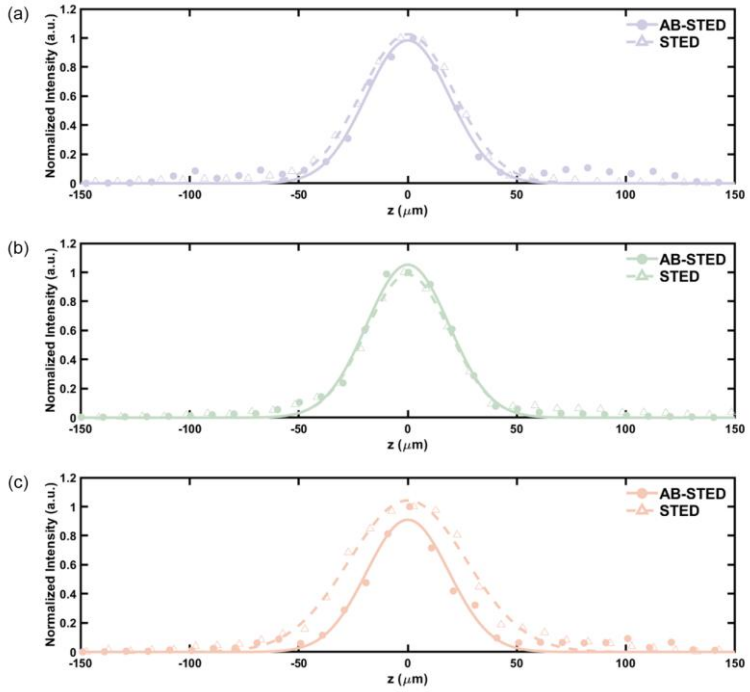
Supplementary Fig. 22. Depth-dependent aspect ratio of nanorods fabricated by axially tuneable Bessel beam based stimulated-emission-depletion (AB-STED) direct laser writing. The aspect ratio of the fabricated nanorods gradually decreases with increasing fabrication depth, while high-aspect-ratio nanostructures are still maintained at depths up to 500 μm (numerical aperture=1.1, working distance=1.5 mm). Points show mean±s.d. (n=5 independently fabricated nanorods per depth).



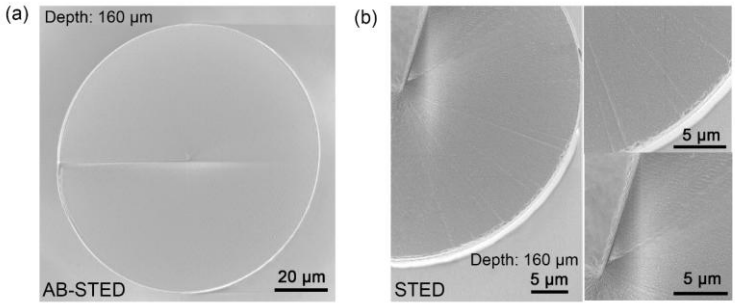
Supplementary Fig. 23. (a) SEM oblique and top views of a 4F system fabricated by axially tuneable Bessel beam based stimulated-emission-depletion (AB-STED) direct laser writing (DLW). (b) SEM image of the 4F system fabricated by STED DLW, showing that the lower surface is larger than the upper one. (c, d) SEM magnified views of the lower surfaces of the 4F systems fabricated by AB-STED and STED DLW. (numerical aperture=1.27, working distance=0.17 mm).



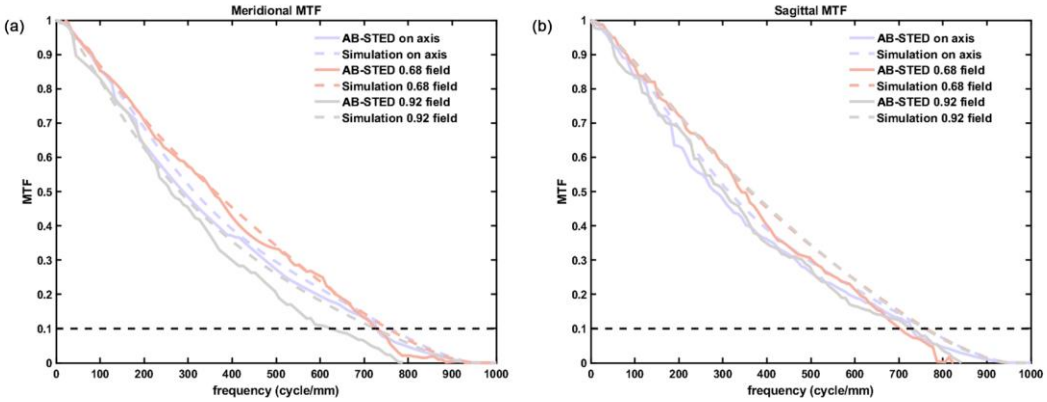
Supplementary Fig. 24. Magnified views of the 4F systems fabricated by stimulated-emission-depletion (STED)direct laser writing, showing a pronounced size mismatch between the upper and lower surfaces (numerical aperture=1.27, working distance=0.17 mm). The green lines mark the measured boundaries of the upper and lower surfaces, and the numerical label reports their size mismatch.



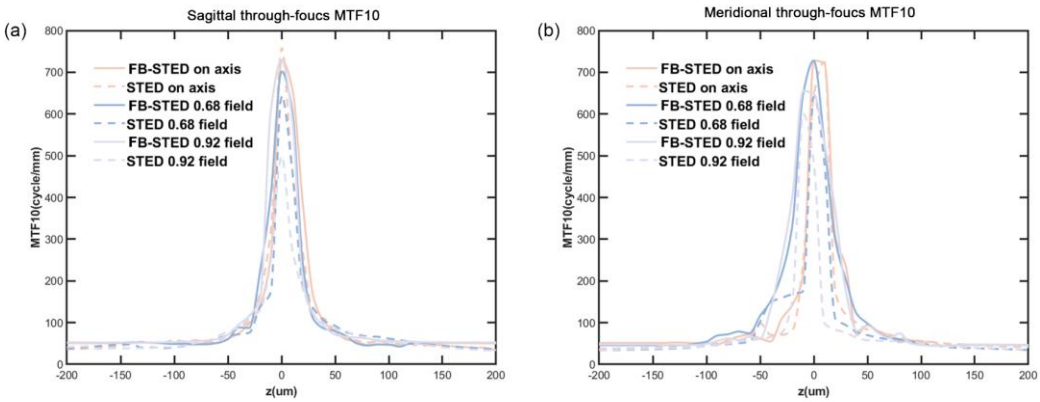
Supplementary Fig. 25. Intensity profiles of the output foci of the 4F systems shown in Fig. 3c. Normalized intensity for incident wavelengths of 405 nm (a), 532 nm (b) and 600 nm (c). Filled circles and solid lines represent the 4F system fabricated by AB-STED DLW; open triangles and dashed lines represent the system fabricated by STED DLW.



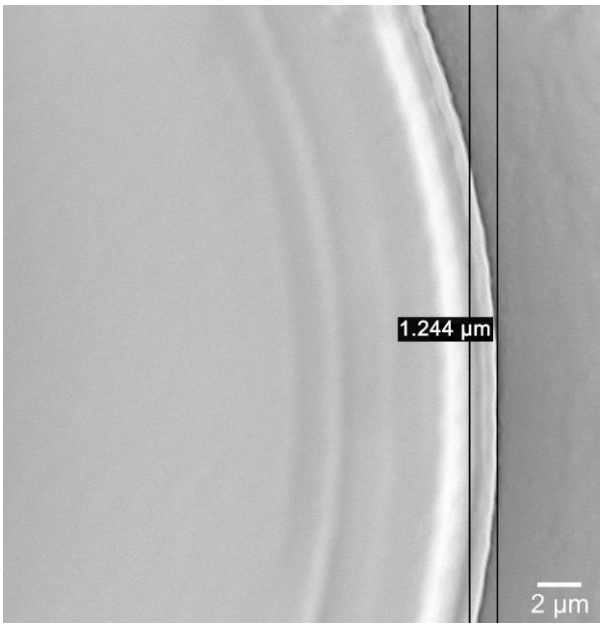
Supplementary Fig. 26. (a) SEM top view of a vortex phase plate (VPP) fabricated by axially tuneable Bessel beam based stimulated-emission-depletion (AB-STED) direct laser writing. (b) SEM magnified view of the VPP fabricated by STED DLW, showing the uneven surface. (numerical aperture=1.27, working distance=0.17 mm).



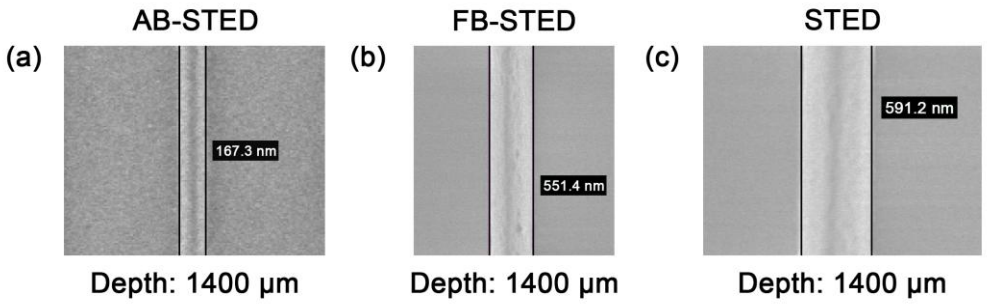
Supplementary Fig. 27. Meridional and sagittal modulation transfer functions curves of the simulated and axially tuneable Bessel beam based stimulated-emission-depletion (AB-STED)-fabricated miniaturized objective lenses. The horizontal black dashed line marks modulation transfer functions=0.1.



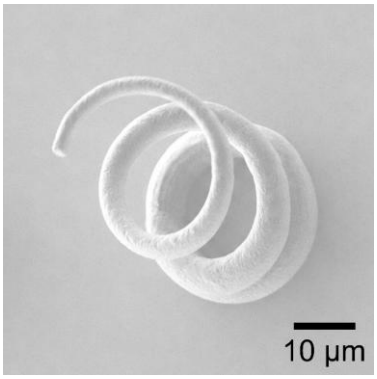
Supplementary Fig. 28. Sagittal and meridional through-focus modulation transfer functions 10 of the miniaturized objective lenses fabricated by axially tuneable Bessel beam based stimulated-emission-depletion (AB-STED) and STED at different field positions. Here, modulation transfer functions 10 denotes the spatial frequency at which the modulation transfer functions decreases to 0.1.



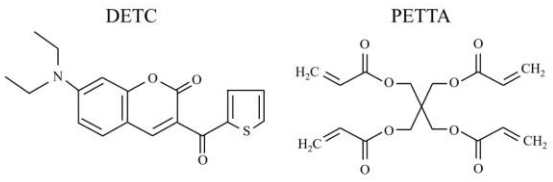
Supplementary Fig. 29. Magnified views of the miniaturized objective lenses fabricated by stimulated-emission-depletion (STED) direct laser writing, showing a pronounced size mismatch between the upper and lower surfaces (numerical aperture=1.27, working distance=0.17 mm). The green lines mark the measured boundaries of the upper and lower surfaces, and the numerical label reports their size mismatch.



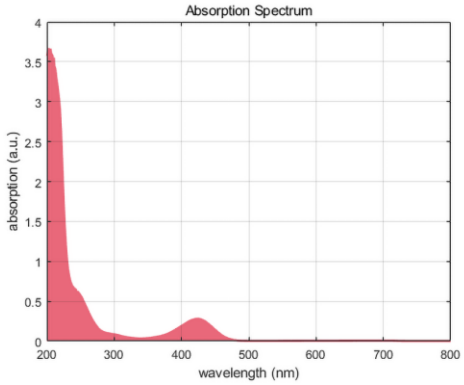
Supplementary Fig. 30. Linewidths obtained by (a) axially tuneable Bessel beam based stimulated-emission-depletion (AB-STED), (b) axicon-based first-order Bessel beam (FB)-STED and (c) STED direct laser writing at a depth of 1400 μm (numerical aperture=1.1, working distance=1.5 mm). The linewidths annotated in the images (167.3, 551.4 and 591.2 nm, respectively) are measurements of the individual lines shown. The corresponding mean±s.d. linewidths from ten independently fabricated lines per method are 167.3±7.9, 554.7±19.1 and 586.1±16.8 nm, respectively.



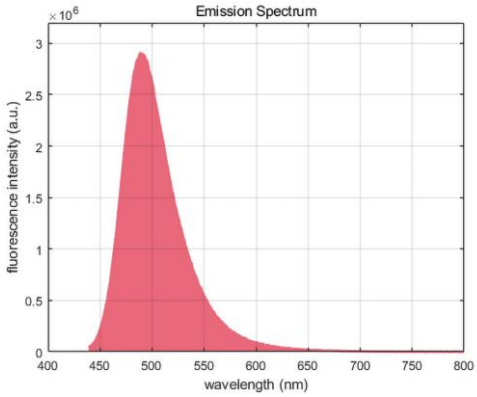
Supplementary Fig. 31. Magnified SEM views of the structures shown in Fig. 5a



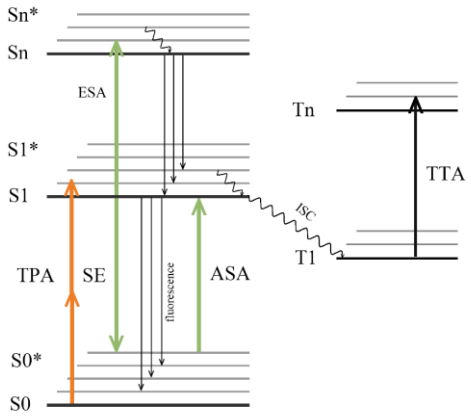
Supplementary Fig. 32. Molecular structures of photoinitiator 7-diethylamino-3-thenoylcoumarin and monomer pentaerythritol tetraacrylate.



Supplementary Fig. 33. Absorption spectrum of photoresist.



Supplementary Fig. 34. Emission spectrum of photoresist.



Supplementary Fig. 35. Energy level of the photoinitiator molecule and schematic illustration of the relevant optical transition processes. S_0: ground state; S_1: first excited singlet state; S_n: higher excited singlet states; T_1 and T_n: triplet states. The depicted processes include two-photon absorption (TPA), stimulated emission (SE), anti-Stokes absorption (ASA), excited-state absorption (ESA), intersystem crossing (ISC), and triplet-triplet annihilation (TTA).

Supplementary Table 1. Simulated axial overlap of axicon- and annular-lens-based Bessel beams with the Gaussian focus.

Depth (μm)	Gaussian focal shift (μm)	Axicon-based Bessel beam non-diffracting axial range (μm)	Relative first-ring intensity of axicon-based Bessel beam at the Gaussian focus	Annular-lens-based Bessel beam non-diffracting axial range (μm)	Relative first-ring intensity of annular-lens-based Bessel beam at the Gaussian focus
160	24.2	-3.8 to 25.4	0.1958	-22.7 to 31.7	0.5260
300	43.9	36.1 to 64.5	0.4328	-4.0 to 54.5	0.5417
500	70.8	91.5 to 121.5	0.0025	23.0 to 87.0	0.5169
750	104.5	160.8 to 191.7	0.0004	56.5 to 127.7	0.5546
1000	138.0	230.7 to 260.3	0.0019	89.7 to 169.2	0.5308
1250	171.6	300.3 to 335.0	0.0001	123.1 to 209.8	0.4662
1400	190.9	341.0 to 377.5	0.0008	146.5 to 232.0	0.4498

Supplementary Table 2. Linewidth comparison at a writing depth of 160 μm (NA = 1.1, WD = 1.5 mm).

Configuration	AO correction	Field type and axial matching status	Post-objective depletion power	Linewidth
STED DLW	No	LG; axially mismatched	8.52 mW	176.7 ± 19.3 nm
AO-STED DLW	Yes	LG; axially matched	8.43 mW	93.6 ± 5.1 nm
FB-STED	No	Bessel; axially matched but not actively tunable	8.90 mW	98.0 ± 3.5 nm
AB-STED	No	Bessel; axially matched and actively tunable	10.32 mW	65.1 ± 1.9 nm
AO-AB-STED	Yes	Bessel; axially matched and actively tunable	10.08 mW	66.3± 2.1 nm

Supplementary Note 1. Debye vector diffraction integral model

In conventional optical field simulations, the Fresnel scalar diffraction method is widely adopted. However, this approach becomes inadequate when describing beam passing through optical elements with high NA, that is, tight focusing conditions. In contrast, the Debye vector diffraction integral model provides an accurate theoretical framework for analyzing optical field distributions in such situations. Therefore, we employ the Debye vector diffraction integral model to simulate the optical field distributions of the depletion beams—including first-order Laguerre–Gaussian (LG), and first-order Bessel beams—in both stimulated emission depletion (STED) direct laser writing (DLW) and axially tunable first-order Bessel-STED (AB-STED) DLW under tight focusing. The validity of the model was confirmed by comparing the simulated and theoretical full width at half maximum (FWHM) of the Gaussian beam.

For high NA systems, the Debye vector diffraction integral theory is well-suited for calculating optical field distributions. Here, we briefly outline its theoretical foundation.

As illustrated in Supplementary Fig. 1, a three-dimensional (3D) Cartesian coordinate system is established with point O as the origin. The position of an arbitrary point P in this coordinate system can be expressed in cylindrical coordinates as $P(\rho_p cos\phi_p, \rho_p sin\phi_p, z_p)$. A medium with refractive index n_1 occupies the region where $z \leq -d$ (indicated by the blue vertical dashed line at $z = -d$), while a medium with refractive index n_2 occupies the region where $z > -d$. The incident light amplitude vector $\overrightarrow{E_0}$, after passing through a high NA lens, is transformed into amplitude vector $\overrightarrow{E_1}$ with wave vector $\overrightarrow{k_1}$. Upon transmission through the dielectric interface at $z = -d$, the amplitude becomes $\overrightarrow{E_2}$ with wave vector $\overrightarrow{k_2}$. Refraction occurs at $z = -d$, where the interface normal is denoted by vector $\vec{s}$. Defining the angle of incidence as θ_1 and the angle of refraction as θ_2, these angles satisfy Snell's law: $n_1 sin\theta_1 = n_2 sin\theta_2$.

The incident light amplitude is expressed as

$$\overrightarrow{E_0} = A_1(\theta_1)\exp(im\Phi) \tag{S1}$$

with the magnitude

$$A_1(\theta_1) = A_0\left(\sqrt{2}\gamma\frac{sin\theta_1}{sin\alpha}\right)^{|m|}\exp\left(-\frac{\gamma^2\sin^2\theta_1}{\sin^2\alpha}\right) \tag{S2}$$

Here, A_0 is scaled according to the actual input power, α is the half-aperture angle (determined by specific experimental parameters), and γ is the truncation parameter, defined as $\gamma = \frac{a_0}{w_0}$, where a_0 denotes the radius of the objective entrance pupil and w_0 represents the beam waist radius. The parameter m is the topological charge ($m = 0$ corresponds to the fundamental Gaussian beam, while $m = 1$ corresponds to the first-order LG beam), Φ is the azimuthal angle in the cylindrical coordinate system, and d denotes the writing depth.

The diffracted field at a point P near the focal region can be expressed as

$$\vec{E}(\vec{p}) = -\frac{in_1 f}{\lambda}\int_0^{\alpha}\int_0^{2\pi} A_1(\theta_1)\sqrt{cos\theta_1}\vec{P}(\theta_1,\phi)A_a(\theta_1,\phi)A_s(\theta_1)A_p(\theta_1,\vec{p})\exp(im\phi)\,sin\theta_1 d\theta_1 d\phi \tag{S3}$$

where $\vec{p} = (\rho_p cos\phi_p, \rho_p sin\phi_p, z_p)^T$ is the coordinate vector of point P, $A_a(\theta_1,\phi)$ represents the aberration introduced by the optical system components. Only the aberration from deep sample

propagation is considered here; hence, it is assumed that $A_a = 1$, indicating the absence of aberration. Sample-induced refractive-index-mismatch aberration was included separately through A_s. $\vec{P}$ can be determined through coordinate transformation of unit vectors, i.e.,

$$\vec{P}(\theta_1, \phi) = \begin{bmatrix} a\left(\tau_p cos\theta_2 \cos^2\phi + \tau_s \sin^2\phi\right) + b\left(\tau_p cos\theta_2 - \tau_s\right) sin\phi cos\phi \\ a\left(\tau_p cos\theta_2 - \tau_s\right) sin\phi cos\phi + b(\tau_p cos\theta_2 \sin^2\phi + \tau_s \cos^2\phi) \\ -a\tau_p sin\theta_2 cos\phi - b\tau_p sin\theta_2 sin\phi \end{bmatrix} \quad (S4)$$

In the Debye model, the polarization state of the incident beam is denoted as (a, b) (analogous to the polarization vectors in the Jones matrix formalism for circularly or linearly polarized light). The Fresnel transmission coefficients, denoted as τ_s and τ_p, can be expressed as:

$$\tau_s = \frac{2sin\theta_2 cos\theta_1}{\sin(\theta_1 + \theta_2)} \quad (S5)$$

$$\tau_p = \frac{2sin\theta_2 cos\theta_1}{\sin(\theta_1 + \theta_2)\cos(\theta_1 - \theta_2)} \quad (S6)$$

$A_s(\theta_1)$ denotes the refractive boundary condition, which is dependent on the depth d of the optical field and accounts for the spherical aberration induced by refractive index mismatch.

$$A_s(\theta_1) = \exp[ikd(n_1 cos\theta_1 - n_2 cos\theta_2)] \quad (S7)$$

$$A_p(\theta_1, \vec{p}) = \exp\left(i\overrightarrow{k_2} \cdot \vec{p}\right) \quad (S8)$$

Substituting equation (S3) gives

$$E_x = aE_{x,x} - bE_{x,y} \quad (S9)$$

$$E_y = aE_{y,x} + bE_{y,y} \quad (S10)$$

$$E_z = aE_{z,x} + bE_{z,y} \quad (S11)$$

Where

$$E_{x,x} = i^m F_m \exp\left(im\phi_p\right) - i^{m+2} F_{m+2} \exp\left[i(m+2)\phi_p\right] - i^{m-2} F_{m-2} \exp\left[i(m-2)\phi_p\right] \quad (S12)$$

$$E_{y,x} = i \cdot i^{m+2} F_{m+2} \exp\left[i(m+2)\phi_p\right] \quad (S13)$$

$$E_{z,x} = -i^{m+1} F_{m+1} \exp\left[i(m+1)\phi_p\right] - i^{m-1} F_{m-1} \exp\left[i(m-1)\phi_p\right] \quad (S14)$$

$$E_{x,y} = -i \cdot i^{m+2} F_{m+2} \exp\left[i(m+2)\phi_p\right] + i \cdot i^{m-2} F_{m-2} \exp\left[i(m-2)\phi_p\right] \quad (S15)$$

$$E_{y,y} = i^m F_m \exp\left(im\phi_p\right) + i^{m+2} F_{m+2} \exp\left[i(m+2)\phi_p\right] + i^{m-2} F_{m-2} \exp\left[i(m-2)\phi_p\right] \quad (S16)$$

$$E_{z,y} = i^{m+1} F_{m+1} \exp\left[i(m+1)\phi_p\right] - i^{m-1} F_{m-1} \exp\left[i(m-1)\phi_p\right] \quad (S17)$$

$$F_m = \int_0^\alpha T(\theta_1)\left[\tau_s + \tau_p cos\theta_2\right] J_m(vsin\theta_1) d\theta_1 \quad (S18)$$

$$F_{m\pm1} = \int_0^\alpha T(\theta_1)\tau_p sin\theta_2 J_{m\pm1}(vsin\theta_1) d\theta_1 \quad (S19)$$

$$F_{m\pm2} = \frac{1}{2}\int_0^\alpha T(\theta_1)\left[\tau_s - \tau_p cos\theta_2\right] J_{m\pm2}(vsin\theta_1) d\theta_1 \quad (S20)$$

$$v = kn_1\rho_p \quad (S21)$$

$$T(\theta_1) = -\frac{i\pi n_1 f}{\lambda} A_1(\theta_1)\sqrt{cos\theta_1} A_S(\theta_1) sin\theta_1 \quad (S22)$$

The optical intensity is subsequently obtained through the relation

$$I = |E_x|^2 + \left|E_y\right|^2 + |E_z|^2 \quad (S23)$$

Supplementary Note 2. Impact of Spherical Aberration on Gaussian Beams

A custom MATLAB program was developed to define the angular variable θ_1 and compute the excitation and depletion beam distributions within the radial range $\rho_p \in [-1 \times 10^{-6}, 1 \times 10^{-6}]m$ at $\phi_p = 0$. To simulate the target optical fields at different depths, the parameter d was adjusted to 50 μm, 100 μm, 150 μm, and 200 μm, respectively. For a topological charge of $m = 0$, the fundamental Gaussian mode distribution was obtained, while for $m = 1$, the first-order LG beam distribution was obtained.

We first simulated the Gaussian beam's optical-field distribution over a range of depths (Supplementary Fig. 2a). Since the excitation power needs to be adjusted to the polymerization threshold at the corresponding depth in subsequent experiments, only the relative intensity distribution is presented here. The optical field distribution of the excitation beam can be described by

$$I = I_0 \exp\left(-\frac{2r^2}{w^2}\right) \quad (S24)$$

where w denotes the beam waist radius, I_0 represents the maximum intensity (i.e., the intensity at the center), and r is the radial distance. As the propagation depth of the Gaussian beam increases, accumulated spherical aberration during propagation leads to a broadening of the beam profile, and the FWHM progressively increases. Meanwhile, owing to the refractive-index mismatch at the water/photoresist interface, the actual Gaussian intensity maximum is axially displaced from the nominal resist focus, i.e., the geometrically defined focal position inside the photoresist. Therefore, in AB-STED DLW, the key requirement is to maintain the spatial overlap between the depletion focal plane and the shifted Gaussian focal plane over an extended axial range. Consequently, if single-beam DLW (i.e., using only the excitation beam) is employed, the theoretical resolution will degrade at greater depths, making it impossible to achieve the same fabrication precision as at the surface.

Supplementary Note 3. Impact of Spherical Aberration on the First-Order LG Beam

We simulated the depth-dependent optical-field distribution of the depletion beam (Supplementary Fig. 3). The depletion beam is a first-order LG beam, which belongs to the family of higher-order Gaussian beams. Its field distribution at the surface is mathematically described by

$$E(r, \varphi, 0) = \left(\frac{\sqrt{2}r}{w_0}\right)^{|l|} L_p^{|l|}\left(\frac{2r^2}{w_0^2}\right) \exp\left(-\frac{r^2}{w_0^2}\right) \exp(-i|l|\varphi) \quad (S25)$$

where r and φ represent the coordinates in the polar coordinate system, w_0 is the beam radius at $z = 0$ (i.e., the beam waist radius), $L_p^{|l|}$ denotes the associated Laguerre polynomial, and l and p are the azimuthal and radial quantum numbers (also referred to as the beam's initial topological charge), respectively. Theoretically, the LG beam features a symmetric "doughnut"-shaped intensity profile with two distinct peaks away from the center. Simulations at increasing depths reveal progressive radial broadening and distortion, accompanied by a notable decrease in intensity. Under spherical aberration,

the peak-to-peak distance expands with depth, and the central hollow region widens, though azimuthal symmetry is largely preserved. These simulated trends agree with theoretical expectations and previously reported behavior[1], supporting the validity of the numerical model. In addition, the LG beam exhibits a pronounced axial shift. At $d = 160\,\mu m$, its center is displaced to $z = 28.5\,\mu m$ (We set $z = 0$ as the position of the Gaussian focus), far exceeding the axial shift of the Gaussian beam. This axial misregistration between the excitation and depletion beams substantially weakens the confinement of the depletion field at the focal region and is one of the main reasons why conventional STED DLW rapidly loses fabrication fidelity at depth.

Supplementary Note 4. Impact of Spherical Aberration on First-Order Bessel Beams Generated by Axicon

In high-NA systems, refractive index mismatch leads to accumulated spherical aberration, which expands the hollow region and distorts the focal spot of LG beams. This degradation limits the ability of STED to maintain super-resolution DLW quality at large depths. Furthermore, this spherical aberration-induced degradation becomes increasingly pronounced with larger refractive index differences between media.

In contrast, Bessel beams exhibit remarkable resistance to scattering, robustness against spherical aberration, and self-reconstruction properties. Their self-recovery capability in heterogeneous media has been shown to improve imaging penetration in scattering samples while reducing artifacts[2]. However, for STED DLW, the key requirement is not only the propagation robustness of the depletion beam itself, but also its spatial overlap with the Gaussian excitation focus at the target writing depth. In addition, a zero-order Bessel beam is not hollow, making it incompatible with STED DLW. We therefore first simulated the optical field distributions of a conventional axicon-based first-order Bessel beam at different sample depths to evaluate whether the axicon-based Bessel depletion field can remain aligned with the Gaussian excitation focus during deep DLW.

In the simulation, the axicon-based first-order Bessel depletion beam was modeled in an end-to-end manner. The axicon and vortex phase pattern on the spatial light modulator (SLM) was first propagated to form a real-space first-order Bessel beam, which was then converted by the Fourier lens into an annular spatial-frequency spectrum and relayed onto the objective entrance pupil. The Debye vector diffraction integral model remains applicable for simulating first-order Bessel beam distributions, though the incident field amplitude requires modification[3].

The relayed pupil field was subsequently used as the input field for the vectorial Debye calculation. To reproduce the deep-writing condition, a flat water/photoresist interface was included, and Snell refraction, Fresnel transmission, and depth-dependent spherical-aberration phase were taken into account. The resulting optical field was calculated inside the photoresist, and the xz distributions together with the xy intensity profiles at the nominal Gaussian excitation focal planes were used to evaluate the axial overlap between the axicon-based Bessel depletion field and the Gaussian excitation focus. Under otherwise identical parameters, simulations were performed to obtain the xz and xy optical-field distributions of the axicon-based first-order Bessel beam at sample depths of 160 μm, 300 μm, 500 μm, 750 μm, 1000 μm, 1250 μm, and 1400 μm, as shown in Supplementary Fig. 4. The simulated Gaussian–Bessel axial overlap was quantified across these depths (Supplementary Table 1).

The axicon-based Bessel beam forms a clear transverse ring-shaped intensity distribution near the designed propagation region and maintains an almost unchanged hollow-ring radius over a large axial range. At shallow depths, such as 160 and 300 μm, the Gaussian focal plane still lies within the effective

non-diffracting region of the axicon-based Bessel beam, where the Bessel intensity remains above the 13% threshold used to define the non-diffracting zone. Therefore, a certain depletion intensity can still be delivered to the Gaussian excitation focus. However, as the fabrication depth increases to 500 μm and beyond, the Gaussian focal plane progressively shifts away from the axial position of the Bessel beam due to depth-induced focal mismatch. Consequently, the Bessel intensity sampled at the Gaussian focal plane decreases sharply to nearly zero, indicating that the axicon-based Bessel beam can no longer provide effective depletion at large depths. This axial mismatch explains the rapid degradation of the STED confinement effect when the axicon-based Bessel beam is used for deep DLW.

Supplementary Note 5. Impact of Spherical Aberration on First-Order Bessel Beams Generated by Annular Lens

The optical-field distribution of the annular-lens-based Bessel beam was simulated using the same end-to-end framework. In this case, the axicon phase was replaced by an annular lens phase on the SLM. Compared with the axicon-based scheme, the annular-lens-based scheme differs by the introduction of an additional Fourier-lens phase, which transforms the phase-modulated beam into an annular pupil field at the objective entrance pupil. The complex field after the SLM was directly relayed to the objective entrance pupil, whereas in the axicon-based scheme the field after the SLM together with an additional Fourier-transform lens was relayed to the objective entrance pupil, and the obtained pupil field was normalized using the same criterion as that used for the axicon case. This relayed pupil field was then used as the input for the same vectorial Debye calculation with the flat water/photoresist interface, including Snell refraction, Fresnel transmission, and the depth-dependent spherical-aberration phase. The resulting xz intensity distributions and the xy intensity profiles at the nominal Gaussian excitation focal planes were calculated at 160 μm, 300 μm, 500 μm, 750 μm, 1000 μm, 1250 μm, and 1400 μm sample depths to evaluate the axial overlap between the annular-lens-based Bessel depletion field and the Gaussian excitation focus, as shown in Supplementary Fig. 5. The simulated results were quantified across these depths (Supplementary Table 1).

Compared with the axicon-based Bessel beam, the annular-lens-based Bessel beam exhibits a much more favorable axial matching behavior with the Gaussian excitation focus. Within the entire simulated axial range from the surface to a depth of 1400 μm, the non-diffracting region of the annular-lens-based Bessel beam remains well overlapped with the aberration-shifted Gaussian focal plane. As a result, the relative first-ring mean intensity sampled at the Gaussian focal plane remains at a relatively stable level over the full depth range. In contrast, the axicon-based Bessel beam rapidly loses its effective overlap with the Gaussian focal plane at depths of 500 μm and beyond, leading to a nearly vanishing depletion intensity at the excitation focus. This sustained Gaussian–Bessel axial overlap ensures that an effective hollow depletion field is maintained at the actual writing plane even at large fabrication depths, providing the optical basis for depth-robust sub-diffraction-limited DLW over a large axial range.

The effective excitation efficiency (effective excitation efficiency = excitation efficiency – excitation efficiency × depletion efficiency) can be obtained by superimposing the excitation field distribution and the depletion efficiency distribution. Point-by-point calculation yields results representative of the final effective point spread function under dual-beam superposition, with the underlying physical concept illustrated in Supplementary Fig. 6. The effective excitation profile remains Gaussian-like at 100 μm (Supplementary Fig. 7), with qualitatively similar behaviour under the other conditions examined. It should be noted that these simulations represent the optical field distribution under dual-beam superposition and do not directly predict the final linewidth. The actual developed linewidth is also

influenced by system aberration and photoresist properties such as two-photon absorption cross-section, polymerization threshold, and molecular diffusion characteristics. Nevertheless, the simulated effective excitation efficiency provides a qualitative comparison of the linewidth achievable with AB-STED versus conventional STED DLW at depth.

At substantial depths, the AB-STED utilizing first-order Bessel beam shows improved super-resolution writing capability, with a precision nearly identical to that at the surface. In contrast, conventional STED DLW using LG beams exhibits severe degradation even under high depletion power. Therefore, we have theoretically demonstrated that the AB-STED DLW employing first-order Bessel beams as depletion beams possesses substantially enhanced deep-sample super-resolution DLW capability compared to conventional STED DLW.

Supplementary Note 6. Adaptive-optics (AO) validation of axial matching and Bessel-enabled tolerance in depth-robust STED DLW

To distinguish the respective roles of excitation–depletion axial matching and Bessel-field topology, we compared five depletion configurations at a writing depth of 160 μm using the same long-working-distance objective lens (NA=1.1, WD=1.5 mm) and otherwise identical fabrication conditions: conventional STED DLW, AO-corrected STED DLW (AO-STED), axicon-based first-order Bessel STED DLW (FB-STED), annular-lens-based Bessel STED DLW (AB-STED), and AO-corrected AB-STED (AO-AB-STED).

6.1 Sensorless AO procedure

A Zernike-modal sensorless AO scheme was implemented to optimize the 532 nm depletion field at the Gaussian excitation focal plane. The 780 nm Gaussian focal plane was first experimentally identified and denoted by z_G. The sample stage was then fixed at this position, and only the phase of the depletion beam was varied during AO optimization. The correction phase applied to the SLM was represented as a linear combination of selected Zernike modes

$$\Phi_{\mathrm{AO}}(\rho,\theta) = \sum_{i=1}^{N} a_i Z_i(\rho,\theta) \tag{S26}$$

where Z_i denotes the i-th Zernike mode and a_i is its corresponding coefficient. In Noll indexing, $Z_4 - Z_{11}$ were used to correct low-order aberrations, while Z_{22} and Z_{37} were included to compensate selected higher-order spherical aberrations. Each mode was normalized to unit root-mean-square (RMS) amplitude over the pupil, such that the corresponding coefficient was expressed in rad RMS. The defocus mode was used to adjust the axial position of the depletion field relative to z_G, while the spherical-aberration modes were used to compensate for depth-induced distortions of the depletion field, and the remaining Zernike modes were used to improve the uniformity of the annular depletion profile.

$$J(\mathrm{a}) = \max_r \left[\frac{1}{N_r} \sum_{(x,y)\in\Omega_r} I(x,y;\mathrm{a}) \right] \tag{S27}$$

where a is the vector of Zernike coefficients, $I(x,y;\mathrm{a})$ is the three-frame-averaged camera intensity, Ω_r denotes a candidate annular region, and N_r is the number of pixels within that region. The total depletion power incident on the SLM was held constant across the five configurations, whereas the post-objective depletion power varied among them, as reported in Supplementary Table 2. The feedback metric therefore quantified the usable annular depletion intensity rather than the total reflected power.

At the beginning of each AO iteration, the feedback metric for the current correction state was remeasured to provide a local reference and reduce the influence of slow laser-power drift. The gradient with respect to each Zernike coefficient was then estimated experimentally by applying symmetric positive and negative modal perturbations. For the i-th mode, the derivative was approximated using a central finite difference

$$\frac{\partial J}{\partial a_i} \approx \frac{J(\mathrm{a} + h_i e_i) - J(\mathrm{a} - h_i e_i)}{2h_i} \tag{S28}$$

where h_i is the perturbation amplitude and e_i denotes the corresponding modal direction. Perturbation amplitudes of 0.5 and 0.25 rad RMS were applied sequentially to balance robustness against experimental fluctuations with sensitivity to local variations near the optimum.

After the gradients for all selected modes were obtained, they were combined into a gradient vector and normalized. The modal coefficients were then updated along the gradient-ascent direction

$$\mathrm{a}_{k+1} = \mathrm{a}_k + \Delta \mathrm{a} \frac{\nabla J}{\|\nabla J\|_2} \tag{S29}$$

where Δa is the update step and $\|\nabla J\|_2$ denotes the L_2 norm of the gradient vector. A candidate correction was accepted only when the measured feedback metric improved relative to the locally remeasured reference. If the coupled gradient update did not improve the metric, the best experimentally measured single-mode perturbation was retained when beneficial; otherwise, the previous correction was preserved. This procedure was iterated to enhance the annular intensity of the depletion pattern without direct wavefront measurement.

In this work, "effective axial matching" is operationally defined as the maximization of the usable depletion-ring intensity at the fixed Gaussian excitation plane z_G. This definition does not imply that the complete 3D intensity distributions of the excitation and depletion fields were independently reconstructed inside the resist. Nevertheless, because the optimization was performed directly at z_G and included the defocus mode, it provides an experimentally relevant measure of excitation–depletion registration at the polymerization plane.

The present sensorless AO implementation has several practical limitations:

(1) Depth-dependent feedback reliability.

The back-reflected depletion doughnut is a double-pass, indirect proxy for the forward depletion field at the writing plane. As the writing depth increases, attenuation and scattering reduce the strength and fidelity of the returned signal. At 160 μm, the feedback remained sufficiently reliable for AO convergence, reducing the STED DLW linewidth from 176.7 ± 19.3 nm to 93.6 ± 5.1 nm. At 300 μm, however, the returned signal became substantially weaker, most likely making it insufficient for reliable optimization. This failure therefore represents a depth-dependent limitation of the present feedback scheme rather than a fundamental depth limit of adaptive optics.

Because our beam-engineering strategy establishes axial registration without requiring a depth-resolved return signal or iterative optimization at each writing depth, it is operationally simpler and more hardware-robust than the present sensorless AO implementation for deep DLW. This comparison is specific to the implemented double-pass feedback architecture; AO approaches using more reliable deep-sample feedback remain complementary and may operate at greater depths.

(2) Experimental and device stability.

Because the metric is intensity-based, laser-power fluctuations can affect gradient estimation. Frame averaging and repeated reference measurements reduce, but do not eliminate, this influence. In addition, the 8-bit phase resolution, calibration errors, and nonlinearity of the SLM limit the precision of the applied correction, particularly near the optimum.

(3) Trade-off between modal coverage and optimization time.

The selected modes Z_4–Z_{11}, Z_{22}, and Z_{37} correct low-order and selected higher-order spherical aberrations but do not fully represent complex sample-induced distortions. Including more modes could improve modal coverage, but would require more sequential measurements, increasing optimization time and sensitivity to slow system drift.

The same single-SLM AO procedure was applied to the STED and AB-STED configurations but not to the FB-STED configuration. In the axicon-based arrangement, the SLM is located at a Fourier plane rather than at a plane conjugate to the objective pupil. Implementing an equivalent pupil-plane AO correction would therefore require an additional pupil-conjugate modulator or a redesigned optical relay. This is a constraint of the present optical implementation and does not indicate a fundamental incompatibility between AO and an axicon-based Bessel depletion beam.

6.2 Linewidth comparison at 160 μm

We first applied the sensorless AO procedure to the LG depletion beam used in conventional STED DLW. During AO optimization of the LG depletion beam, the best-ring mean intensity increased and then converged (Supplementary Fig. 8a). AO correction enhanced the annular component of the back-reflected depletion doughnut (Supplementary Fig. 8b), while the optimized SLM phase combined the vortex and Zernike correction phases (Supplementary Fig. 8c). AO-STED was used to fabricate a representative line (Supplementary Fig. 8d). The same AO procedure was subsequently applied to AB-STED. During AB-STED optimization, the feedback metric fluctuated only slightly (Supplementary Fig. 8f), and a representative line was fabricated (Supplementary Fig. 8g). This limited change is consistent with the annular-lens-based Bessel depletion beam already being effectively registered with the Gaussian excitation plane.

Across the five configurations, linewidths were measured from ten independently fabricated lines per configuration and are reported as mean ± s.d. (Supplementary Table 2). Conventional STED DLW produced a linewidth of 176.7 ± 19.3 nm (this AO dataset was acquired using the long-working-distance objective, NA = 1.1 and WD = 1.5 mm, whereas the 149.1 ± 16.3 nm baseline reported in the main text was obtained separately using the NA = 1.27 and WD = 0.17 mm objective). After AO optimization at the Gaussian focal plane, the linewidth decreased to 93.6 ± 5.1 nm, corresponding to a reduction of approximately 47%. To assess whether the improvement in isolated-line linewidth also benefits complex 2D fabrication, we fabricated line-art reproductions of Vincent van Gogh's The Starry Night using STED and AO-STED DLW at a depth of 160 μm (Supplementary Fig. 8i and 8j, respectively). Compared with STED, AO-STED produced finer lines and more clearly defined local features, providing a qualitative demonstration that optimizing the depletion field at the Gaussian excitation plane improves the fabrication of complex patterns. This substantial improvement demonstrates that restoration of the usable depletion field at the excitation plane is the dominant requirement for achieving effective suppression at depth.

FB-STED DLW produced a linewidth of 98.0 ± 3.5 nm, whereas AB-STED DLW produced a linewidth of 65.1 ± 1.9 nm. Both use first-order Bessel depletion fields, and in both cases the Gaussian excitation

focus falls within the non-diffracting zone at 160 μm. However, at 160 μm the Gaussian excitation focus lies only 1.2 μm from the upper boundary of the FB-STED non-diffracting zone, compared with 7.5 μm for AB-STED (Supplementary Table 1). The simulated relative first-ring intensities at the Gaussian focal plane are 0.1958 and 0.5260, respectively. These results indicate that the FB-STED depletion field has a less favorable axial intensity distribution relative to the Gaussian excitation focus than the AB-STED field at this depth. The measured post-objective depletion powers were 8.90 mW for FB-STED and 10.32 mW for AB-STED. The smaller AB-STED linewidth is therefore consistent with greater usable annular depletion intensity at the Gaussian excitation plane arising from both its more favorable axial field distribution and its higher delivered power. The present comparison does not quantify the separate contribution of each factor. AO correction of AB-STED yielded a similar linewidth of 66.3 ± 2.1 nm at a post-objective depletion power of 10.08 mW. The absence of a measurable additional improvement is consistent with the usable AB-STED depletion zone already being effectively registered with the Gaussian focal plane under these conditions.

The large improvement from LG to AO-LG identifies effective axial registration as the primary factor. AO-STED and AB-STED, however, differed in both field distribution and delivered power (8.43 and 10.32 mW, respectively). Their baseline linewidth difference therefore cannot, by itself, isolate the contribution of Bessel-field topology. The controlled perturbation measurements in Section 6.3 of Supplementary Note 6 provide complementary evidence for the greater tolerance of AB-STED under the tested conditions.

6.3 Tolerance to Axial Misalignment and Spherical Aberration

To confirm that the difference between AO-STED and AB-STED DLW was not caused by failure of the AO procedure, controlled Zernike perturbations were added after AO convergence (Fig. S8e, h). For AO-STED, the optimized coefficient set was defined as zero additional perturbation. The coefficient of Z_4 was then varied from -10 to +10 rad RMS, while all other coefficients were held at their optimized values. The same procedure was applied to AB-STED.

AO-STED exhibited a pronounced maximum in annular-ring intensity near zero additional defocus, followed by a decrease as the magnitude of the perturbation increased. This well-defined maximum supports that the optimized state was close to a local optimum rather than merely terminating because of insufficient feedback sensitivity. The tightly focused LG depletion field is axially localized; therefore, additional wavefront curvature shifts its optimum focal plane away from the Gaussian excitation plane. Consequently, the usable annular depletion intensity at the polymerization plane decreases rapidly even under a moderate residual axial displacement.

In contrast, AB-STED maintained an approximately constant annular-ring intensity over a substantially broader range of added Z_4 coefficients. The Bessel depletion field is formed by the interference of conical-wave components and maintains its annular profile over a finite but extended axial interval. Adding moderate defocus modifies the axial location and intensity distribution of this extended field, but does not immediately move the fixed Gaussian excitation plane outside the usable Bessel zone. The Gaussian focus can therefore remain within a high-intensity portion of the Bessel depletion field even when the depletion phase deviates from its optimized value. This produces a broad intensity plateau rather than the narrow optimum observed for AO-STED.

To determine whether the broader optical-field response of AB-STED translates directly into greater fabrication tolerance, we measured linewidths while independently varying the added Z_4 and Z_{11} coefficients over the expanded range of −50 to +50 rad RMS (Supplementary Fig. 9). These measurements distinguish the effects of two different residual wavefront errors. Z_4 predominantly probes

sensitivity to relative axial displacement between the excitation and depletion fields, whereas Z_{11} probes degradation caused by a radially varying spherical-aberration phase. Under Z_4 defocus (Supplementary Fig. 9a), AO-STED reached its minimum linewidth near zero additional perturbation, whereas the linewidth increased rapidly for both positive and negative coefficients. This response reflects the axially localized nature of the LG depletion field: Z_4 predominantly changes the wavefront curvature and displaces the optimum depletion plane from the Gaussian excitation focus, thereby rapidly reducing the usable annular depletion intensity within the polymerization volume. AB-STED showed markedly greater tolerance to both Z_4 defocus and Z_{11} primary spherical-aberration perturbations than AO-STED, although its linewidth gradually increased under large Z_4 perturbations, particularly for negative coefficients. Thus, the expanded sweep reveals the onset of linewidth degradation for AB-STED under strong defocus, while showing that it retains a narrower linewidth than AO-STED throughout the tested range. Because the Gaussian excitation focus remained within the extended non-diffracting zone of the Bessel depletion field, moderate relative axial displacement did not immediately remove the effective annular depletion intensity from the writing plane.

Under Z_{11} perturbation (Supplementary Fig. 9b), the AO-STED linewidth again increased away from its minimum near zero, whereas the AB-STED linewidth changed only slightly across the examined range. The tolerance limit of AB-STED to this imposed spherical-aberration mode was therefore not reached at ± 50 rad RMS. A contribution from depletion saturation to the nearly flat Z_{11} linewidth response at the depletion power used here cannot be excluded. Unlike defocus, Z_{11} introduces a radially dependent pupil-phase error that redistributes and distorts the depletion field rather than predominantly translating its focal plane. AB-STED again maintained an approximately constant linewidth across the same perturbation range. This response is consistent with the annular-lens-based Bessel depletion field providing enhanced tolerance not only to residual axial misregistration, but also to moderate spherical-aberration-induced wavefront distortion.

The broad response of AB-STED on both Z_4 and Z_{11} also explains why applying AO to the uncorrected AB-STED configuration produced little additional linewidth improvement at 160 μm. The annular-lens phase had already positioned the Gaussian excitation plane within the extended high-intensity region of the Bessel depletion field, while the extended conical-wave field remained effective under moderate residual defocus and spherical aberration. Small additional corrections did not substantially increase the usable depletion-ring intensity at the writing plane. Thus, the limited improvement after AO does not indicate that the AO procedure was ineffective; instead, it indicates that AB-STED was already operating within a broad axial-matching plateau. Nevertheless, the gradual broadening under strong Z_4 defocus demonstrates that the axial tolerance is finite, while the limit for the tested Z_{11} perturbation remains undetermined.

These measurements distinguish two related but different contributions. Effective axial matching determines whether sufficient depletion intensity is present at the Gaussian excitation plane and is therefore the primary requirement for linewidth reduction. Once this condition is established, the extended Bessel field broadens the range of relative axial positions over which effective depletion is maintained, reducing sensitivity to residual defocus, focal drift, and imperfect excitation–depletion registration. The Bessel topology therefore provides additional axial tolerance and enhanced robustness to residual aberrations, rather than replacing the requirement for axial matching.

Taken together with the depth-dependent comparisons in Supplementary Notes 4 and 5, these experiments lead to a revised physical and methodological interpretation of deep STED DLW. The advance is not a generic substitution of an LG depletion beam by a first-order Bessel mode. An axicon-

based Bessel field can retain an extended non-diffracting region, but if that region becomes displaced from the aberration-shifted Gaussian excitation focus, the usable annular depletion intensity within the polymerization volume approaches zero. Conversely, restoring an LG depletion field at the Gaussian plane through AO substantially improves suppression, demonstrating that axial registration is the primary requirement. However, the AO-corrected LG field remains axially localized, whereas the matched Bessel field maintains effective annular depletion over a broader range of relative axial positions. Axial matching and Bessel topology therefore play distinct but complementary roles: the former determines whether effective depletion is available, and the latter determines how robustly that condition is retained against residual displacement and spherical-aberration-induced field distortion.

The conventional configurations examined here do not readily provide these two properties simultaneously. The axicon configuration principally controls the Bessel cone angle through the effective axicon period, which couples the transverse ring size, non-diffracting range and axial field distribution and consequently provides limited flexibility for maintaining registration over a continuously increasing writing depth. AO could in principle be combined with an axicon-based Bessel field, but in our present optical arrangement the beam-shaping SLM is located at a Fourier plane rather than a plane conjugate to the objective pupil. Applying an equivalent pupil-plane correction would therefore require an additional pupil-conjugate modulator or a redesigned optical relay. In contrast, AO correction of the conventional LG field can be implemented on the existing pupil-conjugate SLM, but our current sensorless optimization relies on a double-pass return signal whose strength and reliability decrease with depth.

AB-STED integrates programmable axial positioning and an extended first-order Bessel depletion zone within the same deterministic beam-generation strategy. The annular spectral radius predominantly controls the transverse spatial-frequency distribution and depletion-ring geometry, while the effective focal length controls the axial position and formation range of the Bessel field. Their joint adjustment enables the usable depletion zone to be positioned around the depth-shifted Gaussian excitation focus without requiring depth-resolved feedback and iterative modal optimization at every writing plane. The extended Bessel topology then provides tolerance to residual focal displacement after this registration has been established. To the best of our knowledge, this specific integration of axial registration and extended Bessel depletion has not previously been established in either STED microscopy or STED DLW. It converts a fixed Bessel mode into a depth-addressable depletion field and provides the physical basis for extending super-resolution DLW from shallow regions to axially extended and millimeter-depth fabrication.

Supplementary References

1. S. Deng, L. Liu, Y. Cheng, et al., "Investigation of the influence of the aberration induced by a plane interface on STED microscopy". Optics Express 17, 1714-1725 (2009).
2. F. O. Fahrbach, P. Simon and A. Rohrbach, "Microscopy with self-reconstructing beams". Nature Photonics 4, 780-785 (2010).
3. H. Gong, G. Li, Q. Chen, et al., "Research on an Algorithm for Rapid Realization of Light Field Transmission". Acta Optica Sinica 36, 60-64 (2016).